The Astrophysical Journal, 924:37 (12pp), 2022 January 1 https://doi.org/10.3847/1538-4357/ac323b

Cometary Activity beyond the Planets

Naceur Bouziani[1] and David Jewitt[2,3]
[1] Center of Research in Astronomy, Astrophysics and Geophysics, Route de l'Observatoire, 16340 Bouzareah, Algiers, Algeria; naceur.bouziani@craag.edu.dz
[2] Department of Earth, Planetary and Space Sciences, University of California, 595 Charles Young Drive East, Los Angeles, CA 90095-1567, USA
[3] Department of Physics and Astronomy, University of California, 430 Portola Plaza, Box 951547, Los Angeles, CA 90095-1547, USA
Received 2021 February 4; revised 2021 October 18; accepted 2021 October 20; published 2022 January 10

Abstract

Recent observations show activity in long-period comet C/2017 K2 at heliocentric distances beyond the orbit of Uranus. With this as motivation, we constructed a simple model that takes a detailed account of gas transport modes and simulates the time-dependent sublimation of supervolatile ice from beneath a porous mantle on an incoming cometary nucleus. The model reveals a localized increase in carbon monoxide (CO) sublimation close to heliocentric distance $r_H = 150$ au (local blackbody temperature ∼23 K), followed by a plateau and then a slow increase in activity toward smaller distances. This localized increase occurs as heat transport in the nucleus transitions between two regimes characterized by the rising temperature of the CO front at larger distances and nearly isothermal CO at smaller distances. As this transition is a general property of sublimation through a porous mantle, we predict that future observations of sufficient sensitivity will show that inbound comets (and interstellar interlopers) will exhibit activity at distances far beyond the planetary region of the solar system.

Unified Astronomy Thesaurus concepts: Long period comets (933); Comet nuclei (2160); Oort cloud (1157)

1. Introduction

It has long been known that some comets are active far beyond the range of heliocentric distances over which water ice can sublimate, the latter corresponding roughly to the region interior to Jupiter's orbit (semimajor axis 5 au). The interpretation of activity in distant comets is complicated. Ices more volatile than water (e.g., CO, CO_2) may be involved, as might the exothermic crystallization of amorphous water ice, at least at distances $r_H \lesssim 12$ au (Jewitt 2009; Guilbert-Lepoutre et al. 2012). In comets observed after perihelion, the origin of distant activity is further complicated by the slow conduction into the interior of heat acquired at perihelion, resulting in the delayed activation of subsurface volatiles and driving distant outbursts (e.g., Prialnik & Bar-Nun 1992).

Significantly, in long-period comets that are active at large distances while still inbound to perihelion, the conduction of perihelion heat can play no role. The long-period comet C/2017 K2 (PANSTARRS), which was discovered to be active preperihelion at heliocentric distance $r_H = 16$ au, falls into this category. Observations reveal a spherical coma of large (∼0.1–1 mm) grains, slowly ejected (speeds of ∼4 m s^{-1}) close to a steady state from a nucleus no more than 9 km in radius (Jewitt et al. 2017, 2019a). A coma was present in prediscovery observations at 23.8 au, a linear extrapolation of photometry indicates that activity began at $r_H \sim 26$ au (Jewitt et al. 2019a), and more detailed considerations indicate that C/2017 K2 was active at ∼35 au (Jewitt et al. 2021). Comet C/2010 U3 (Boattini) likewise possessed a coma at 25.8 au preperihelion (Hui et al. 2019), while C/2014 B1 (Schwartz) was also active far beyond the water sublimation zone with a coma of large, slowly moving grains but observed only starting at 11.9 au, preperihelion (Jewitt et al. 2019b). Recently, comet C/2014 UN271 (Bernardinelli-Bernstein) was reported to be active at 23.8 AU (Farnham 2021) and may have been active at much larger distances.

Free sublimation of exposed supervolatile ices provides an initially attractive but ultimately unsatisfactory explanation for the distant activity. Gas drag forces produced by free sublimation of CO in equilibrium with sunlight at distances >15 au are orders of magnitude too small to eject 100 μm particles against the gravity of the nucleus (Jewitt et al. 2019a). Nor could smaller particles be ejected owing to interparticle (van der Waals) cohesive forces occurring naturally between grains. Taken at face value, this "cohesion bottleneck" prevents the ejection of particles of any size in distant comets, as noted by Gundlach et al. (2015). However, sublimation in a confined space, for example, beneath a porous refractory mantle, offers the possibility of building the pressure to values much higher than those reached in free sublimation to space. Fulle et al. (2020) suggested that sublimation occurs within centimeter-sized "pebbles" whose small but finite strength allows gas pressure to build up to values sufficient to eject dust by gas drag. Activity driven by the crystallization of amorphous water ice has also been proposed as a mechanism, but, at ⩾15 au, temperatures are too low for this process to occur.

Here we explore solutions to the bottleneck problem involving the buildup of pressure by the sublimation of subsurface ice, taking careful account of the processes by which heat and gas transport occur. In so doing, we find that cometary activity is possible at extraordinarily large distances, even far beyond the planetary region of the solar system. We present the model in Section (2) and the results in Section (3).

2. The Model

The physical model we present is a refinement of Whipple's (1950) icy conglomerate model, enhanced to include the presence of a nonvolatile, low-conductivity porous mantle (see Figure 1). In active comets, such a "rubble mantle" is produced by fallback of suborbital particles and volatile loss from the strongly heated surface. In inactive comets—for example, those in the Oort cloud and Kuiper Belt storage reservoirs—an

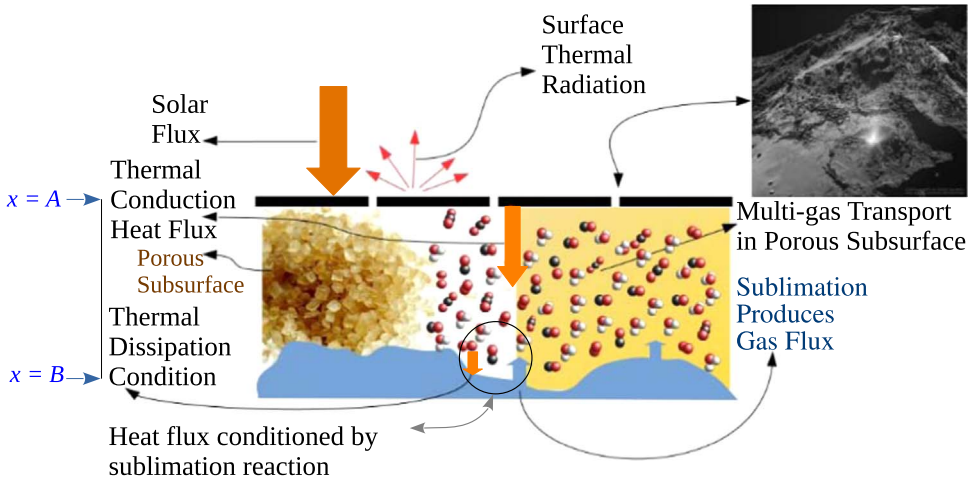

Figure 1. Schematic of the model physics. The photo on the right is from the ESA Rosetta Mission to 67P/Churyumov-Gerasimenko (Osiris Team), and the one on the left is sugar powder from J. C. M. https://stock.adobe.com/contributor/265923/jcm.

irradiation mantle can grow as pure ices are rendered nonvolatile by prolonged exposure to cosmic rays (Kaiser & Roessler 1997; Mayo Greenberg 2002; Abplanalp et al. 2019; Gautier et al. 2020). In our model, we assume that a nonvolatile mantle of variable thickness and porosity overlies CO ice.

In equilibrium with sunlight, the energy balance averaged over the surface of a spherical, isothermal nucleus is written as

$$\frac{F_{\odot}(1-A_{\rm B})}{r_H^2}+4\sigma\epsilon_{\rm IR}T_{\rm OC}^4=4\sigma\epsilon_{\rm IR}T^4+4k(T)\frac{\partial T}{\partial x}. \quad (1)$$

The first term on the left-hand side of Equation (1), in which $F_{\odot}$ is the solar constant, r_H is the heliocentric distance in au, and $A_{\rm B}$ is the Bond albedo, represents the absorbed solar power. The second term on the left, only important at the largest heliocentric distances, accounts for heating of the nucleus from other external sources. These include the cosmic microwave radiation background and the integrated light of the stars, as represented by an effective temperature $T_{\rm OC}=10$ K. The emissivity of the nucleus is $\epsilon_{\rm IR}$, while σ is the Stefan–Boltzmann constant. On the right, the first term is the flux of radiation from the nucleus surface at temperature T, while the second term is the conducted flux. There is no contribution from sublimation, since the surface layers are assumed to be volatile-free.

The conductivity in Equation (1), $k(T)$, is written as in Mendis & Brin (1977),

$$k(T)=A+B(4\sigma\epsilon_{\rm IR}T^3), \quad (2)$$

where the first term, A, is the effective thermal conductivity of the porous mantle, and the second term accounts for radiative conductivity. Here, B is an empirical attenuation factor for the radiative conduction of void and adjacent grain surfaces within the porous medium.

As shown schematically in Figure 1, the ice is not on the surface, as in Whipple's model, but hidden under a mantle. Energy propagated through the mantle to deeper layers can trigger the sublimation of buried ices. At the ice–mantle interface, the conducted energy flux sublimates ice at a rate

$$k(T)\frac{\partial T}{\partial x}=E_{\rm CO}f_{\rm CO}, \quad (3)$$

in which we ignore heat conducted into the "cold core" beneath the sublimation front. A justification of this neglect is given in the Appendix.

Here the sublimation is entirely controlled by the conducted heat: a nonequilibrium process. The generated gas is also subject to another nonequilibrium process caused by the pressure gradient. The heat is driven down the temperature gradient toward the ice front, B, in Figure 1, while the gas is driven up toward the surface of the comet, A, by the pressure gradient established in the porous medium. In this simple comet model, the reverse flow of molecules is not favored, so condensation is somewhat unlikely. The sublimation flux that was calculated in Watson et al. (1961) and Delsemme & Miller (1971) approximates the sublimation flux in our case too. Otherwise, we should model the condensation process and calculate the net flux:

$$f_{\rm CO}=P(T)\sqrt{\frac{1}{2\pi k_B Tm}}. \quad (4)$$

Practically, $f_{\rm CO}$ is an upper limit to the sublimated flux because of the possibility of backflow and sticking of molecules reflected from particles above the ice front. This is the necessary Neumann boundary condition. At all levels above the ice front, we calculate the net flux, $J_{\rm CO}$, formed as molecules diffuse through the porous medium.

In Equation (4), $P(T)$ is the equilibrium pressure of the CO gas over the CO ice as a function of temperature. Here $P(T)$ contains valuable information about both the gas and the ice structure. We consider sublimation and condensation as facets of a single process that is a first-order phase transition phenomenon. It is worthwhile to invoke the chemical reaction formalism to address it. Sublimation is considered as the direct process, while condensation is the reverse process, analogous to the direct and reverse arrows between reactants and products in chemical reaction theory. Usually, experiments are conducted in closed thermodynamic equilibrium to characterize the chemical reaction and find the equilibrium constant called $K(T)$. We found that for pure ice, the temperature dependence of $P(T)$ follows the Arrhenius equation below Equation (5) just like $K(T)$ in the language of chemical reactions. The similarity arises because in a chemical reaction, we consider the breakage of bonds within molecules, while in sublimation, the breaking

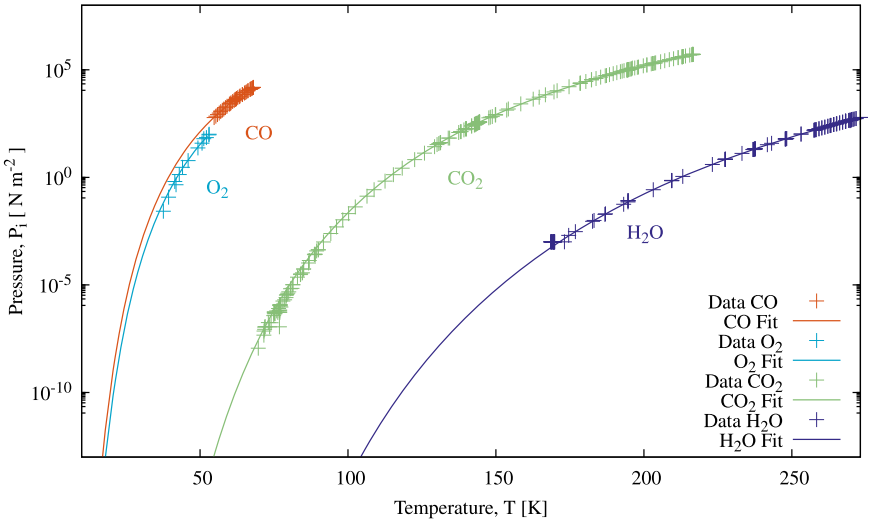

Figure 2. Sublimation pressures from Fray & Schmitt (2009) fitted by the relation $P_i(T) = A_i e^{-E_i/\mathrm{RT}}$ to determine the activation energy, E_i (J mol^{-1}), and the frequency factor, A_i. The resulting numerical values are listed in Table 1.

bonds are those between molecules. For this reason, the activation energies E_i in the sublimation case are small compared to the energies involved in chemical reactions.

We fitted

$$P(T) = A_{\mathrm{CO}} e^{-\frac{E_{\mathrm{CO}}}{RT}}, \tag{5}$$

where R is the molar gas constant, E_{CO} is the activation energy of CO sublimation, and A_{CO} is a constant, using nonlinear Levenberg–Marquardt fits to sublimation data from Fray & Schmitt (2009). The data and fits are shown in Figure 2.

We find that Equation (5) provides a better fit to the data than the polynomials used by Fray & Schmitt (2009). We succeeded in inferring the activation energy of CO with exceptional accuracy (see the energies actually measured using various dedicated experimental methods), and we did this independently and in a temperature range not included in the data (Luna et al. 2014).

Our model is governed by two coupled partial differential equations, one for heat transport,

$$\rho c_p(T)\frac{\partial T}{\partial t} = \frac{\partial}{\partial x}\left(k(T)\frac{\partial T}{\partial x}\right), \tag{6}$$

and one for mass transport,

$$\frac{\partial n}{\partial t} = \epsilon\frac{\partial}{\partial x}\left(D_K\frac{\partial n}{\partial x} + \frac{\kappa n}{\mu}\frac{\partial p}{\partial x}\right). \tag{7}$$

In Equation (6), ρ is the density and $k(T)$ is the conductivity at temperature T, while t is the time, x is the depth in the nucleus, and $c_p(T)$ (see Equations (8) and (9)) is the heat capacity of the mantle. In Equation (7), $D_K = \frac{r_p}{3}V_{\mathrm{th}}$ is the Knudsen diffusion coefficient, $V_{\mathrm{th}} = \sqrt{\frac{8k_BT}{\pi m}}$ is the thermal speed, $\kappa = \frac{r_p^2}{32}$ is the permeability of the porous medium (Cussler 2009), and $\mu = \frac{\alpha}{\pi^{3/2}}\frac{\sqrt{k_BmT}}{\sigma^2}$ is the dynamic viscosity. Other quantities are k_{B}, the Boltzmann constant; α, a numerical constant on the order of 1; T, the temperature; σ, the CO molecule's collision diameter; m, the CO molecular mass; p, the CO gas pressure $p(n, T) = nk_{\mathrm{B}}T$; n, the molecular density of CO; r_p, the pore radius; and ϵ, the porosity.

The equations are coupled with the transport coefficients. Water ice acts as a mineral at the low temperatures found in the outer solar system, so we neglect the H_2O gas flux and focus only on the CO flux using a simplified version of the model described in Bouziani & Fanale (1998). Gas produced by sublimation passes through the porous mantle toward the comet surface. Figure 3 illustrates the various modeled mechanisms of gas transport inside the porous mantle. This model takes into account both microscopic and macroscopic behavior and also treats the interaction between the gas and the walls. It provides a continuous physical modeling of the coupling between mechanisms—from discontinuous collisions to the collective macroscopic behavior of continuous matter—and thus the prediction of the mass flow rate and pressure distribution with reasonable accuracy over the widest range of gas pressures. The model depends only on molecular data and fundamental parameters such as temperature, composition, and total pressure. This approach allows us to address the thermal and dynamical coupling of comets in a continuous and physical way. Table 1 summarizes the parameters used in the numerical simulations.

We assume that the dust mantle is composed of a mixture of refractory minerals and water ice. To estimate the heat capacity of the ice, we use the heat capacity c_p deduced from the data provided in Shulman (2004),

$$c_p(\mathrm{ice}) = 7.73T(1 - e^{-1.263\times10^{-3}T^2}) \times(1 + e^{-3\sqrt{T}} \times 8.47T^6 + 2.0825 \times 10^{-7}T^4e^{-4.97\times10^2T}), \tag{8}$$

while for the refractory part of the mantle, we use the data for enstatite found in Krupka et al. (1985). We find that the Shulman equation gives an excellent representation of the data at both high and low temperatures. We assume a water ice/dust ratio = 1 and thus take the specific heat capacity of the mixture as the average of Equations (8) and (9),

$$c_p(\mathrm{dust}) = 2.03T(1 - e^{-2.5\times10^{-4}T^2})(1 + e^{-8.53\times10^{-1}\sqrt{T}} \times1.24\times10^{-09}T^6 - 3.69 \times 10^6T^4e^{-4.76\times10^5T}), \tag{9}$$

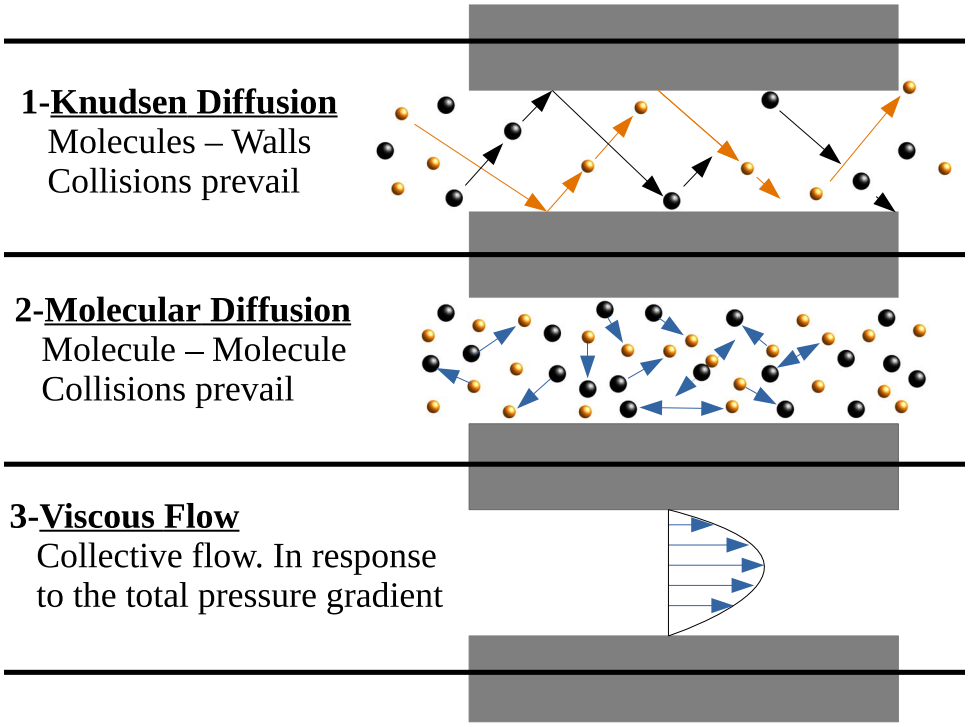

Figure 3. Schematic showing different molecular transport modes. In the porous mantle, gas transport is hindered by the walls encountered by the molecules during their journey. Panels (1)–(3) show the three gas transport mechanisms within the porous mantle. This figure is adapted from https://tinyurl.com/y3xyj9ss.

Table 1
Physical Parameters

Parameters	Symbols	Values	References
Oort cloud temperature (K)	$T_{\rm OC}$	10	Baxter et al. (2018)
Gravitational constant ($m^3\ kg^{-1}\ s^{-2}$)	G	6.67×10^{-11}	
Comet nucleus surface albedo	A_B	0.04	
Comet nucleus radius (m)	r_n	9×10^3	Jewitt et al. (2017)
Comet nucleus density (kg m^{-3})	ρ_n	533	
Dust grain density (kg m^{-3})	$\rho = \rho_n$	533	
Porous crust thickness (m)	L	10^{-2}–10^2	
Main pore radius (m)	r_p	10^{-8}–10^{-2}	
Porosity	ϵ	0.80	
Emissivity	$\epsilon_{\rm IR}$	0.95	
Stefan–Boltzmann constant ($W\ m^{-2}\ K^{-4}$)	σ	5.67×10^{-8}	
Solar constant ($W\ m^{-2}$)	$F_\odot$	1360.8	
Boltzmann constant ($J\ K^{-1}$)	k_B	1.380649×10^{-23}	
Ideal gas constant ($J\ K^{-1}\ mol^{-1}$)	R	8.314	
Latent heat–CO ($J\ mol^{-1}$)	$E_{\rm CO}$	7.45×10^3	Data and fits Figure 2
Sublimation pressure of CO ($N\ m^{-2}$)	$P(T)$	$8 \times 10^9 e^{-7450/RT}$	Data and fits Figure 2
Thermal conductivity ($W\ m^{-1}\ K^{-1}$)	$k(T) = A + B(4\sigma\epsilon_{\rm IR}T^3)$	A and $B = 10^{-4}$–10^{-1}	Mendis & Brin (1977)

where c_p is expressed in $J\ kg^{-1}\ K^{-1}$. We assume a water ice/dust ratio = 1 and thus take the specific heat capacity of the mixture as the average of Equations (8) and (9). Figure 4 shows how the heat capacity of the mantle c_p depends on the temperature.

We solved Equations (6) and (7) as a function of time, following the motion of comet C/2017 K2 upon its approach to the Sun from large heliocentric distances. For this purpose, we used the barycentric orbital elements from Królikowska & Dybczyński (2018) while noting that the current Sun-centered orbit from NASA's Horizons ephemeris software[4] is slightly hyperbolic (eccentricity $e = 1.0004$, versus $e = 0.9999$ from Królikowska & Dybczyński 2018). This difference between the barycentric and Sun-centered elements is negligible for our purposes. The model solves the heat (Equation (6)) and gas transport (Equation (7)) equations in a coupled manner. As it approaches the Sun, the surface temperature of C/2017 K2 increases from the limiting interstellar value of 10 K to higher temperatures, creating a temperature gradient within the mantle and driving conduction toward the buried ice layer. Heating of the ice triggers sublimation, producing a pressure gradient and

[4] http://ssd.jpl.nasa.gov/horizons.cgi

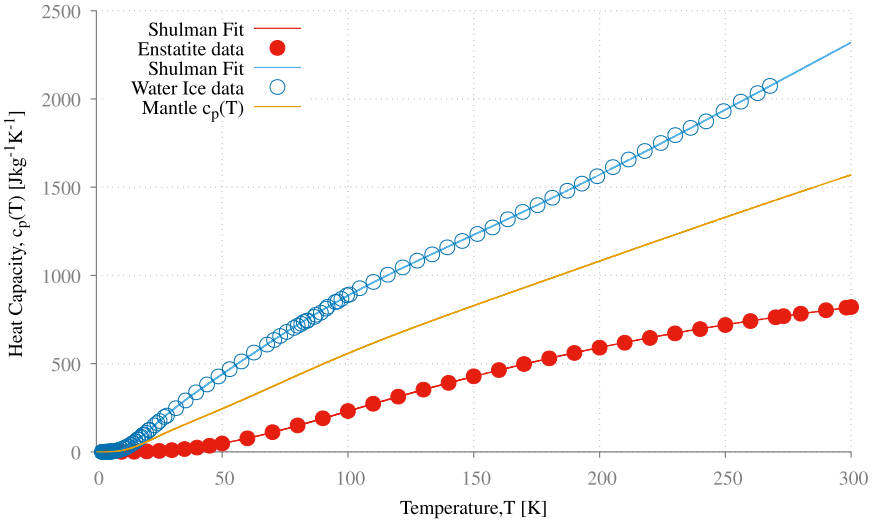

Figure 4. Heat capacity of the mantle as a function of temperature, $c_p(T)$, in J kg^{-1} K^{-1}.

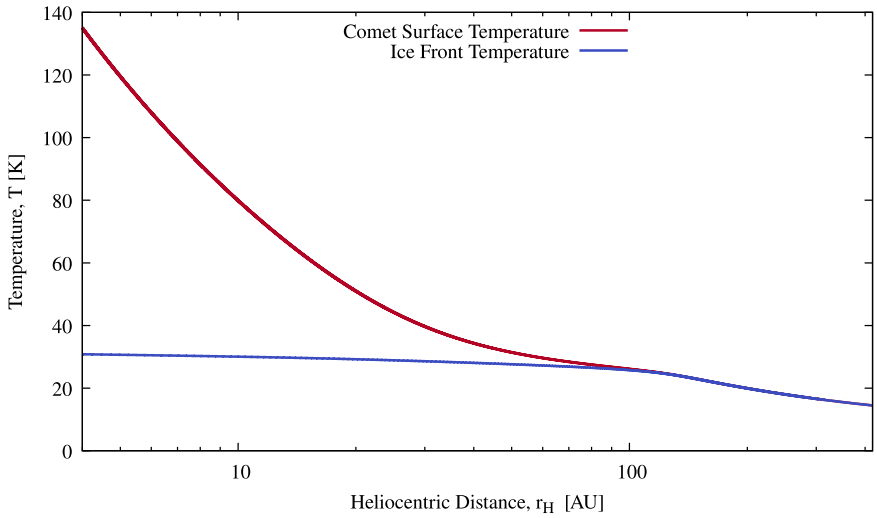

Figure 5. Nucleus surface (red line) and buried ice front (blue line) temperatures as a function of heliocentric distance for infalling comet C/2017 K2. In this illustrative example, the effective thermal conductivity is $k(T) = 10^{-2}$ W m^{-1} K^{-1}, the pore radius is $r_p = 10^{-4}$ m, 30% of the flux is allowed to escape the mantle, and the mantle thickness is 1 m.

resulting in a diffusive flow of gas toward the comet's surface, eventually leading to escape and the expulsion of embedded dust particles through gas drag. The downward conduction of heat and upward transport of sublimated gas molecules are characterized by distinct and different timescales, each dependent on the thermal and microphysical properties of the material, as we will discuss in Section 3.2. The boundary condition (Equation (1)) is time-dependent because the orbital position is a function of time.

3. Results and Discussion

3.1. The Activity Mechanism

Figure 5 shows that the surface temperature increases, as expected from radiative equilibrium, in proportion to $r_H^{-1/2}$. On the other hand, the temperature at the ice–mantle boundary at first rises as r_H decreases (we refer to this region as regime 1) but becomes nearly constant at $r_H \lesssim 150$ au (regime 2). This flattening occurs because the heat conducted to the ice–mantle boundary in region 2 is almost entirely used to break intermolecular bonds in the ice, leaving little to raise the temperature. These qualitatively different temperature-versus-distance trends were first noted for H_2O by Mendis & Brin (1977) for Comet Kohoutek (1973f) and later by Prialnik & Bar-Nun (1988). The model confirms this behavior and extends it to much larger heliocentric distances in more volatile ices. For convenience, in the remainder of this paper, we refer to the junction between region 1 and region 2 as the "Mendis point." The CO flux coming out from the comet mantle is given by Equation (7). In order to better understand the orbital behavior of this flux as the comet approaches the Sun, we solve the coupled Equations (6) and (7) and focus on the averaged flux $J_{\rm CO}$ by estimating the difference in the value of a variable between the surface of the comet A and the base of the mantle B; this approximation is emphasized in Section 3.2. In doing so, we deliberately ignore the local variation of this flux within the mantle. The flux $J_{\rm CO}$ is

$$J_{\rm CO} = \epsilon\left(D_K\frac{dn}{dx} + \frac{\kappa n}{\mu}\frac{dp(n,T)}{dx}\right). \quad (10)$$

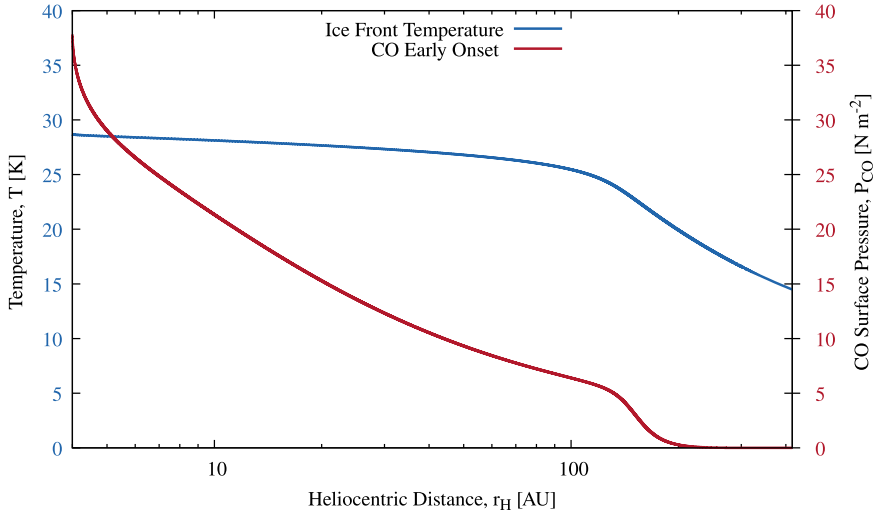

Figure 6. The CO ice front temperature (blue line) and pressure just below the surface, p_{CO} (red line), the latter showing the Mendis point at about 150 au. This simulation assumes thermal conductivity $k(T) = 10^{-4}$ W m^{-1} K^{-1} and a mantle thickness of 1 m. The comet surface pores are 10% smaller than the mantle pores, which have $r_p = 1.15 \times 10^{-4}$ m.

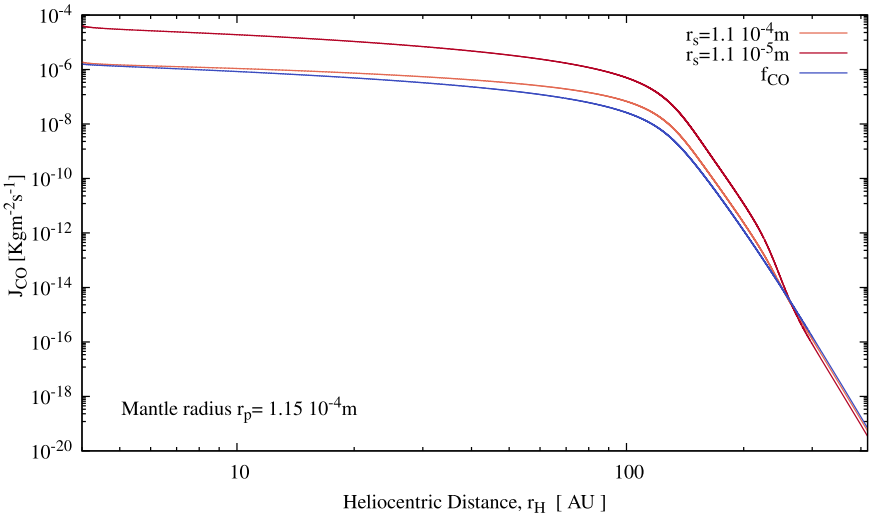

Figure 7. The CO main flux J_{CO} as a function of heliocentric distance for two surface pore radii, r_s. The mantle pore radius is $r_p = 1.15 \times 10^{-4}$ m. The assumed thermal conductivity is $k(T) = 10^{-3}$ W m^{-1} K^{-1}; the mantle thickness is 1 m.

Equation (10) shows how Knudsen free diffusion combines with collective viscous flow (also called Hagen–Poiseuille flow in fluid dynamics). Although these two flows are additive, they are not independent of each other. They are coupled through the pregradient coefficients thanks to the microscopic approach of the model, which integrates the walls in the collision from the very beginning.

Figure 6 shows the CO gas pressure just below the surface, p_{CO}, as a function of r_H. We find a prominent local bump in p_{CO} at $r_H \approx 150$ au, corresponding to the Mendis point. Further exploration shows that the location and amplitude of the J_{CO} bump depend on several physical parameters, including the assumed active surface fraction of the mantle (the comet surface structure) and the mantle thickness. For example, Figure 7 shows that the amplitude of the Mendis point bump increases as the mantle active surface fraction decreases, because a smaller surface pore radius (r_s) increases the overall flow velocity and allows the buildup of higher pressures that, in turn, speed up the flux even more (viscous mode being faster). Figure 8 shows, as expected, that flux J_{CO} increases as the mantle thickness decreases; while thinner mantles provide less impedance to the flow of gas, they also allow higher temperatures, and so higher pressures, at the ice sublimation front.

The steady increase in J_{CO} after the 150 au Mendis point becomes an abrupt rise as the comet approaches the Sun (see Figure 9). Part of this strong increase at small r_H is due to the rising contribution of the radiative term to the effective thermal conductivity of the mantle. To demonstrate this behavior, we show in Figure 9 the effect of arbitrarily removing the radiative term by setting $B = 0$ in Equation (2). In this model with a 5 m thick mantle, the CO flux J_{CO} at 4 au falls from 6.4×10^{-7} kg m^{-2} s^{-1} (blue curve; including radiative term) to $\approx 1.2 \times 10^{-7}$ kg m^{-2} s^{-1} (red curve; no radiative term). Figures 6–9 reveal that, depending on the assumed parameters of the mantle, radiative conduction begins to be significant around 50 au and reaches its maximum near perihelion but has no effect at distances corresponding to the CO Mendis point.

Why is there a local pressure bump near $r_H = 150$ au (see Figure 6) and not a continuous rise toward smaller heliocentric

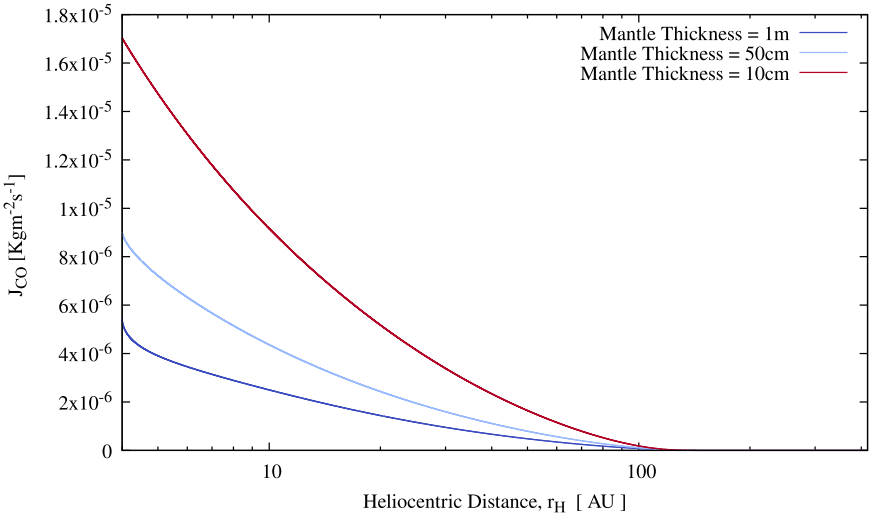

Figure 8. Dependence of the CO main flux J_{CO} on heliocentric distance and the assumed mantle thickness.

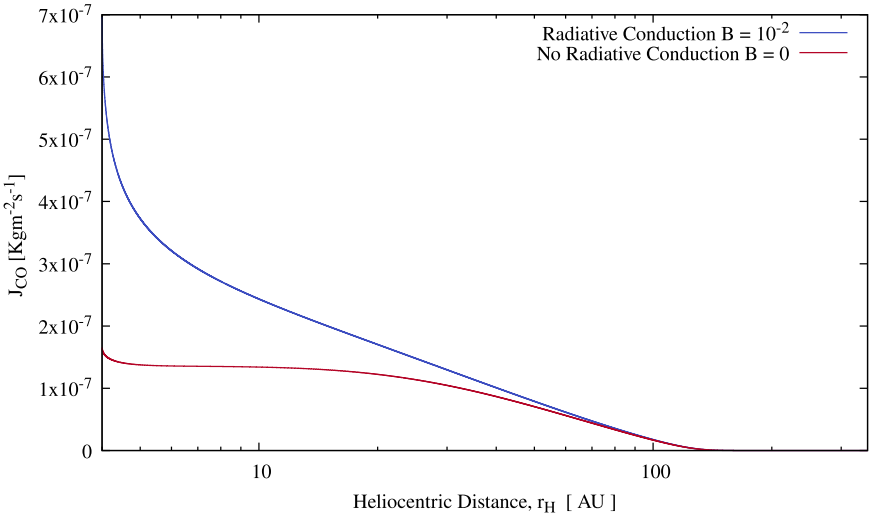

Figure 9. Effective of radiative conduction. The blue curve shows the J_{CO} flux when thermal conductivity includes a radiative contribution as described in the text. The red curve shows the surface pressure calculated without a radiative contribution. Here the mantle thickness is 5 m. All other parameters are held fixed between the models.

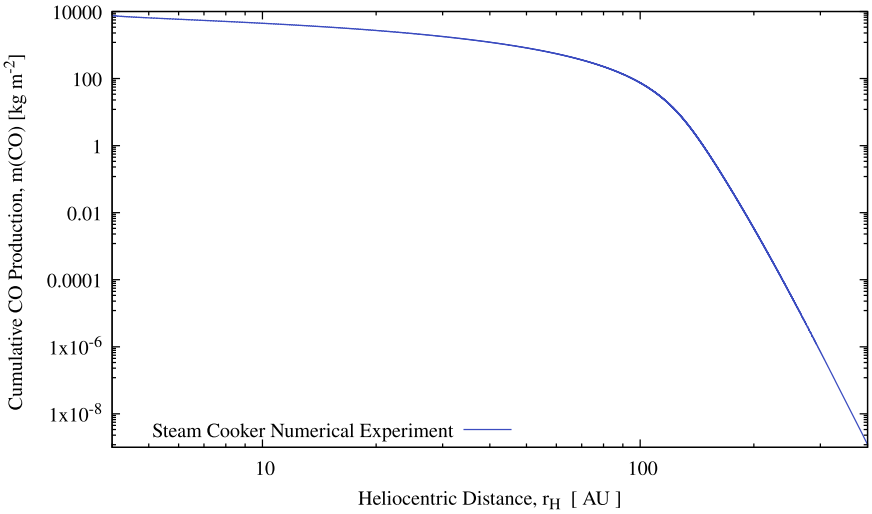

Figure 10. Extreme case of a totally sealed surface (steam-cooker approximation). This shows the cumulative CO gas mass production in kg m^{-2}. For this numerical experiment, we used $k(T) = 10^{-2}$ W m^{-1} K^{-1}, and the mantle thickness is 1 m. The curve is independent of the mantle structure.

distances? Our models give several clues. First, consider the unlikely case of a totally sealed comet surface (the "steam-cooker" approximation). Figure 10 shows that, as expected, the calculated pressure closely follows the temperature of the ice with no pressure bump and independent of the adopted physical parameters of the mantle. This numerical experiment gives the total cumulative CO gas production on the whole path, mainly produced after the CO Mendis point. The steam-cooker approximation proves that the bump and changes inward of the Mendis point are products of gas transport processes in the mantle because these fall to zero when the surface is sealed. Second, apart from this pathological case, which we do not expect to find in nature, the pressure bump exists in all models, albeit with widely different amplitudes depending on the model parameters, even in the case of an almost totally (99%) permeable mantle. Prialnik & Sierks (2017) noted that the uppermost surface layer of the mantle may be less permeable to flow than the deeper layers. We model this by reducing the comet surface pore radii, r_s, compared to the mantle pore radii, r_p. Figure 7 shows that the flux $J_{\rm CO}$ amplitude and behavior are strongly controlled by the assumed structural properties of the comet mantle. The more the flux is inhibited, the higher the flux bump is. The location of the Mendis point at the junction between the two thermal regimes was noted above. It is at this confluence point that the lower flow entering the mantle ($x = B$ in Figure 1) stops increasing over time and slowly becomes constant in response to the flattening of the temperature dependence caused by strong CO sublimation in regime 2. This happens while, at the surface of the comet ($x = A$ in Figure 1)—and in the mantle, depending on the pore radius—the gas pressure remains high. The transition from the rising ice front temperature in regime 1 to the nearly constant ice front temperature in regime 2 leads to a temporary undersupply of CO at the base of the mantle relative to the loss rate from the surface, creating a local maximum as in Figure 6 and, also in Figure 7, see the orange curve. The width of the bump is a measure of the mantle's holding or response time. The undersupply of CO starting around 150 au relative to the rate of loss from the surface is responsible for the peak as the mantle switches from regime 1 to regime 2.

3.2. Retention Timescale

The porous mantle of the comet acts as a buffer to the gas flow produced by sublimation at the bottom. In order to understand this buffer and explore the physical parameters that affect the gas retention time, we estimate in this section the timescale corresponding to this buffer.

We first define the Knudsen number K_n as

$$K_n = \frac{\lambda}{r_p}, \tag{11}$$

where r_p is the pore radius, and the mean free path is given by

$$\lambda = \frac{1}{\sqrt{2}\,\pi\sigma^2 n}. \tag{12}$$

Here σ is the effective particle radius, and n is the number density in the gas. The Knudsen number gives a measure of the importance of gas–gas collisions relative to gas–particle collisions, with the solid material making up the porous mantle.

We define an effective flow velocity of the CO gas through the mantle, V, from $V = J_{\rm CO}/n$, where n is the gas number density. Then, if ΔL is the mantle thickness, Equation (10) can be rewritten as

$$V = \frac{\epsilon D_K}{n}\frac{\Delta n}{\Delta L} + \frac{\epsilon\kappa}{\mu}\frac{\Delta p}{\Delta L}. \tag{13}$$

The time taken for the flow to cross ΔL defines a holding or retention timescale, $\tau = \frac{\Delta L}{V}$. Equation (13) gives

$$\tau = \frac{\mu n \Delta L^2}{\epsilon\kappa n \Delta p(n, T) + \epsilon D_K \mu \Delta n}. \tag{14}$$

Here $\Delta p = (p_A - p_B)$ and $\Delta n = (n_A - n_B)$ are the differences in pressure and gas density, respectively, between the surface of the comet (level A in Figure 1) and the bottom of the mantle (level B). For simplicity, we calculate the intermediate coefficients D_K, μ, and λ of this equation using the averaged value of temperature, molecular density, and pressure (i.e., $T_m = \frac{T_A + T_B}{2}$).

Equation (14) shows that τ is governed by the two main modes of gas transport, namely, (1) Knudsen diffusion in the second denominator term and (2) viscous flow (first denominator term). Figure 11 illustrates these two modes, as well as the transition and slip stages that are intermediate steps between them over the wide range of pressures and pore sizes. The Knudsen number approximately indicates the ranges of the different modes.

At what heliocentric distance does the Knudsen–viscous transition occur? The answer will depend on the structure of the dust mantle, in particular the pore radius and the average free path, λ, which varies with pressure. Figure (12) shows how the retention time changes with the heliocentric distance, r_H, focusing on the coupling between the Knudsen flow and the viscous flow and the different steps between the two flows. It reveals two very distinct configurations. At large r_H, we find an almost constant timescale of one century, leading to a slow and almost uniform motion of the gas leaving the comet surface at a global bulk flow velocity of $V = \frac{1}{3}\,10^{-9}$ m s^{-1}. The retention timescale decreases dramatically as the comet approaches the Sun, falling to about an hour at 50 au. This indicates an acceleration of the gas, which we approximate by estimating the slope of Figure 12, given the assumed physical parameters. By examining the behavior of the retention time (Figure 13), we can easily identify the four known modes for each independently computed Knudsen number value, and this is then a check of the model. The model was able to capture the complete physics of the flow without any artificial intervention by using the Knudsen number to switch from one mode to the other.

Knudsen diffusion predominates mainly at low pressure, and the model allows a viscous flow to develop continuously when the pressure becomes appreciable. As we produce gas by sublimation, Figure (14) shows that, depending on the transport mode, the duration of this retention time can vary widely.

3.3. Largest Ejected Dust Particle

To be ejected, a dust particle must first overcome the cohesive forces, S_0, exerted on it by the surrounding dust material (Gundlach et al. 2015). The minimum size of the

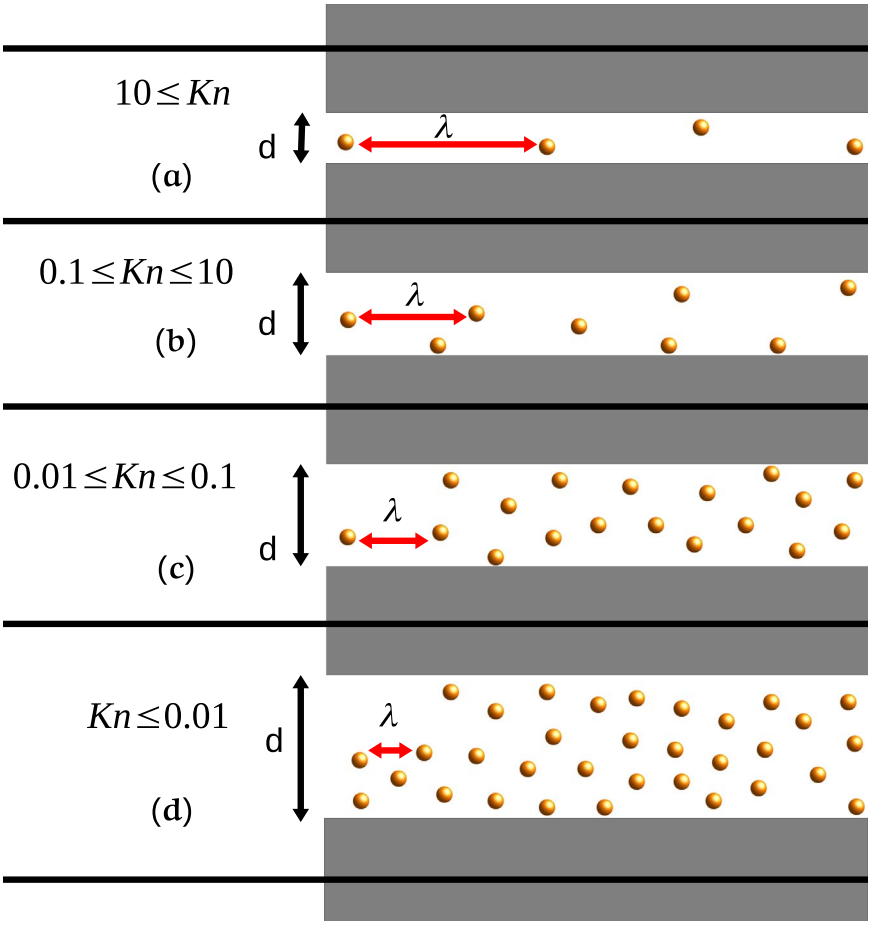

Figure 11. TheF diagram shows how the different gas transport processes should evolve as the comet moves from the Oort cloud to the inner solar system, going from high K_n numbers ($K_n = \lambda/d$, where λ is the mean free path and d is the pore size) to low K_n numbers and changing continuously over a wide range. Flow regimes evolve from Knudsen free diffusion (a), followed by a transition regime (b) that turns into a slip regime (c) that leads to a viscous continuum regime (d). Figure modified from Moghaddam & Jamiolahmady (2016) and https://tinyurl.com/y3xyj9ss.

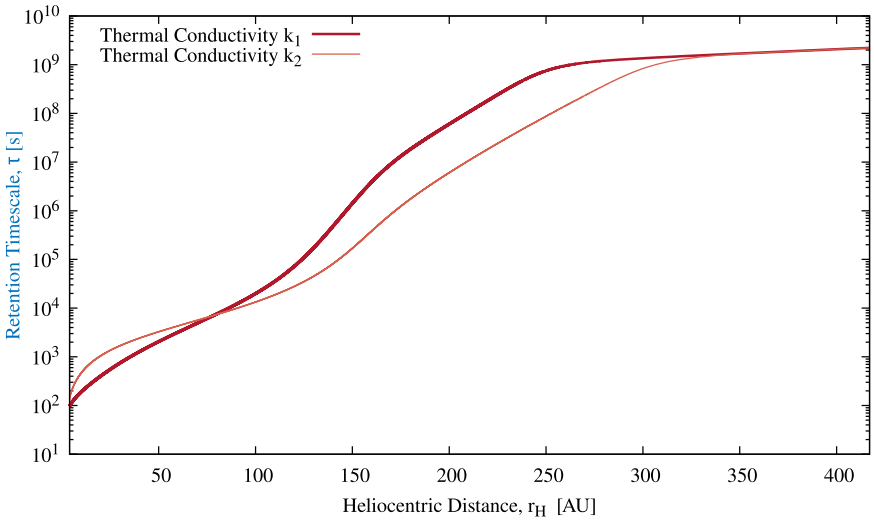

Figure 12. Retention timescale τ (Equation (14)) vs. the heliocentric distance r_H for two thermal conductivities (in W m^{-1} K^{-1}): (1) $k_1(T) = 10^{-2} + 10^{-2}(4\sigma_{\rm IR}T^3)$ and (2) $k_2(T) = 10^{-4} + 10^{-2}(4\sigma_{\rm IR}T^3)$.

grains that could escape is (Jewitt et al. 2019a)

$$a_s(r_H) = \frac{S_0}{C_D f_s(r_H) V_s(r_H)}, \qquad (15)$$

where C_D is a dimensionless constant of order unity, f_s (kg m^{-2} s^{-1}) is the mass sublimation flux, and V_s is the speed of the sublimated gas. Once detached, the dust grain needs a force to accelerate above escape velocity. This force can be provided by gas drag. For particles that are spherical and of uniform density,

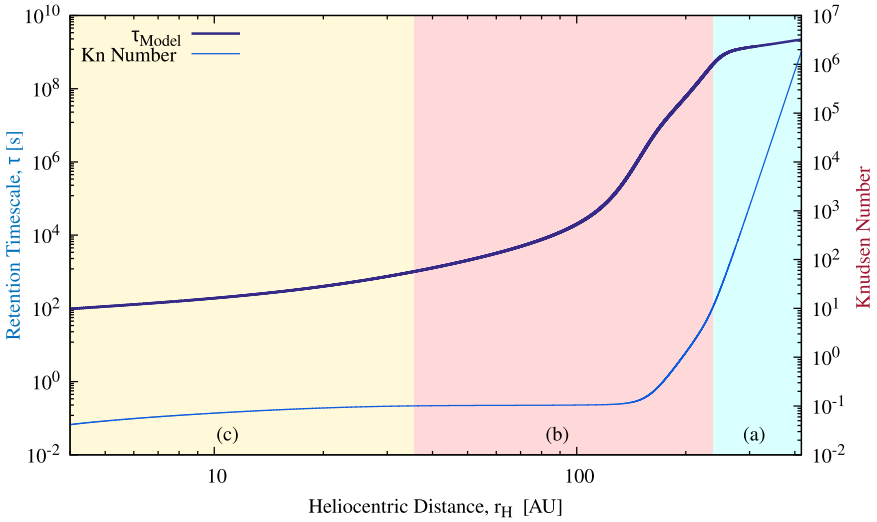

Figure 13. This figure shows the retention time ($\tau_{\rm Model}$; thick line) in various transport modes. The Knudsen number (thin line) is shown on the right axis. Shaded area (a) is the Knudsen diffusion region ($10 \leqslant K_n$), (b) is the transition regime ($0.1 \leqslant K_n \leqslant 10$), and (c) is the slip regime region, where $0.01 \leqslant K_n \leqslant 0.1$. For purposes of illustration, we have assumed a thermal conductivity $k(T) = 10^{-2} + 10^{-2}(4\sigma_{\rm IR}T^3)$ (W m^{-1} K^{-1}) and a mantle pore radius $r_p = 10^{-4}$ m, and comet surface pores are taken to be equal to 95% r_p.

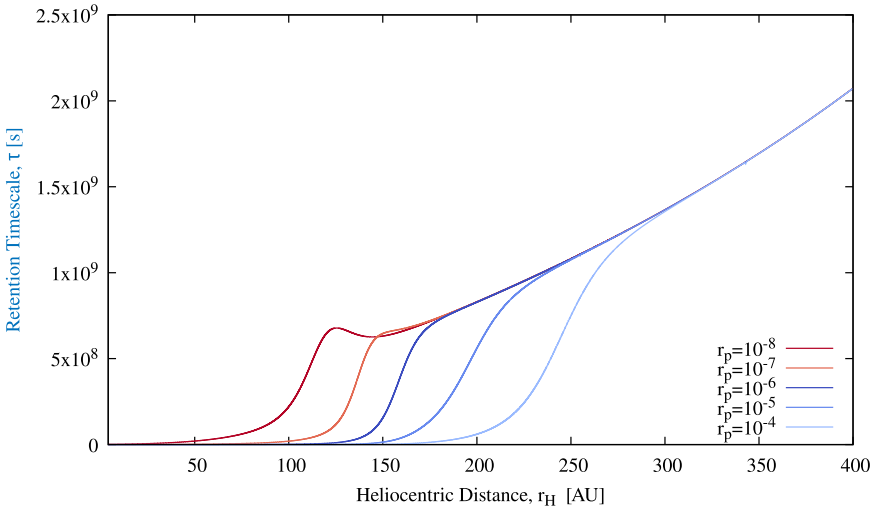

Figure 14. Effect of pore radius on retention time (Equation (14)). The curves show that the behavior of τ changes depending on whether the transition (Knudsen–viscous) in the gas transport occurs before (blue curves) or after (red curves) the 150 au Mendis point. It is shown here that the sublimation temperature transition has an important retention effect, and this effect scales with r^2. We have assumed that $k(T) = 10^{-2} + 10^{-2}(4\sigma_{\rm IR}T^3)$ (W m^{-1} K^{-1}), with a mantle thickness of 1 m and surface pore radii $r_s = 0.95r_m$.

the maximum size of grains that can be ejected is approximated by Jewitt et al. (2019a):

$$a_c(r_H) = \frac{9C_D f_s(r_H) V_s(r_H)}{16\pi G\rho\rho_n r_n}. \quad (16)$$

Here $a_s(r_H)$ and $a_c(r_H)$ are the dust grain sizes escaping the comet surface against cohesive forces and cometary gravity, respectively. The model outputs f_s(CO) and $V_s(CO) = \sqrt{\frac{8k_B T_s}{\pi\mu m_H}}$ are, respectively, the CO gas outflow and its thermal speed taken at the comet surface, where T_s is the comet surface temperature; μ is the molecular weight; $m_{\rm H}$ is the mass of hydrogen; G is the gravitational constant; $\rho = \rho_n$ are, respectively, the dust and nucleus densities; C_D is the dimensionless drag efficiency coefficient, assumed to be equal to 1; the cohesive strength constant $S_0 \approx 1.5 \times 10^{-4}$ N m^{-1} (Sánchez & Scheeres 2014); and r_n is the comet nucleus radius.

Figure 15 displays Equations (15) and (16) as a function of r_H. Particle radii must lie above the red curve in order for gas drag to exceed intergrain cohesive forces and below the blue curve for gas drag to exceed the gravitational pull of the nucleus. The figure shows that these conditions can be simultaneously satisfied at all distances inside the $r_H \sim 150$ au CO Mendis point, thus presenting a resolution of the cohesion bottleneck problem for all active comets observed to date.

4. Summary

We present a detailed gas physics model of the sublimation of cometary CO ice buried beneath a permeable, refractory dust mantle. The model is solved as a function of time and distance along the orbit of the distantly active long-period comet C/2017 K2.

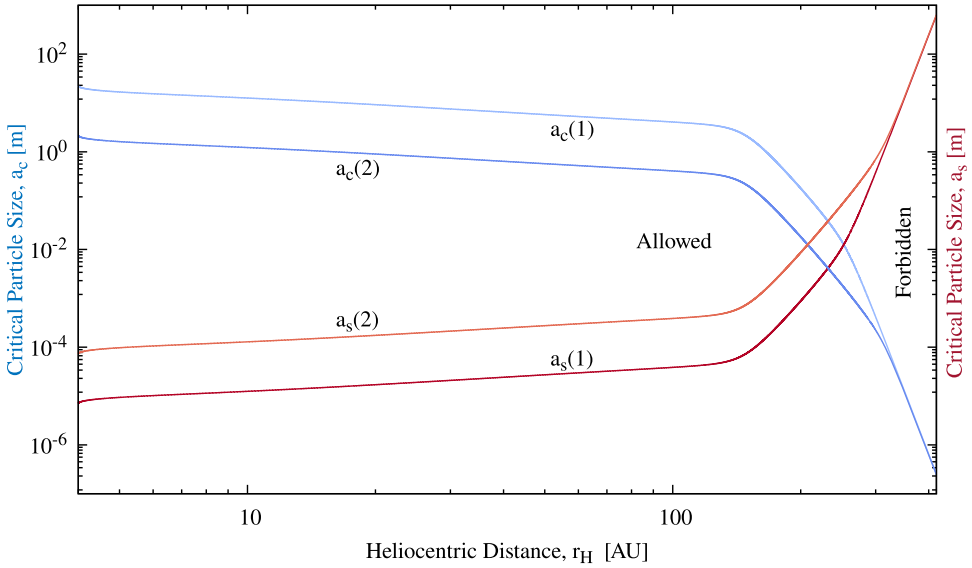

Figure 15. Largest dust particle escaping the comet surface. The forbidden and allowed zones for dust particle production are separated by the bottleneck intersection point. The critical sizes a_c and a_s are labeled (1) and (2) to show the effect of mantle pore sizes; (1) r_p is 10^{-4} m and (2) r_p is 10^{-3} m, and thermal conductivity is $k(T) = 10^{-4}$ W m^{-1} K^{-1}. We observe on this figure that for $r_p = 10^{-3}$ m, we cannot overcome cohesion and detach 0.1 mm dust particles (see the inner curves $a_c(2)$ and $a_s(2)$) unless we reach a heliocentric distance of 5 au. The assumed thickness of the mantle is 1 m, and the surface pores have radii $r_s = 0.97 r_p$.

1. Our main result is that we find an unexpected local peak in CO production at very large heliocentric distances ($r_H \approx 150$ au), caused by the buildup of pressure beneath a permeable mantle of modest thickness.
2. This peak, whose magnitude is a function of several mantle microphysical parameters, corresponds to the Mendis point, where the buried CO ice front transitions between distinct temperature regimes.
3. While modeled on C/2017 K2 as a specific case, our conclusions are general. Comets entering the solar system from the Oort cloud and interstellar distances may become active far beyond the planets, at heliocentric distances $r_h \sim 150$ au. Observational attempts to detect such ultradistant activity are encouraged.

We thank the anonymous referee for the valuable comments. We thank B. Schmitt and N. Fray for providing the empirical pressure–temperature data for cometary ices.

Appendix

To justify our neglect of conduction into the cold core beneath the sublimation front (Equation (3)), we can show that sublimation dominates the energy budget over conduction down into the cold core. If l is the thermal skin depth to the cold core, then

$$l \sim \left(\frac{k\tau}{\rho c_p}\right)^{1/2}. \quad \text{(A1)}$$

Here k is the thermal conductivity of the material, and ρ and c_p are, respectively, the density and heat capacity. The quantity τ is the heating timescale.

The conducted heat flux into the cold core is $F_C = k(dT/dx) \approx k\Delta T/l$, where $\Delta T = T_{CO} - T_C$ is the temperature difference between the top and bottom of the heated layer of thickness l. Then,

$$F_C = \left(\frac{k\rho c_p}{\tau}\right)^{1/2} \Delta T. \quad \text{(A2)}$$

For comparison, the energy flux used by sublimation is

$$F_{\rm sub} = f_{\rm CO} L, \quad \text{(A3)}$$

where $f_{\rm CO}$ is the mass flux of CO in kg m^{-2} s^{-1}, and $L = 2.66 \times 10^5$ J kg^{-1} is the latent heat of CO from Table 1.

Conduction into the cold core is smaller than sublimation when $F_C < F_{\rm sub}$, leading to

$$f_{\rm CO} > \left(\frac{k\rho c_p}{\tau}\right)^{1/2} \frac{\Delta T}{L}. \quad \text{(A4)}$$

Setting $\Delta T = (26 - 10) = 16$ K, $k = 10^{-3}$ W m^{-1} K^{-1}, $\rho = 533$ kg m^{-3}, $c_p = 119$ J kg^{-1} K^{-1}, and $\tau \approx 5 \times 10^9$ s as the travel time from the Mendis point to 10 au, we find that sublimation dominates provided $f_{\rm CO} > 6.7 \times 10^{-9}$ kg m^{-2} s^{-1}. For comparison, Equation (4) gives $f_{\rm CO} = 1.4 \times 10^{-7}$ kg m^{-2} s^{-1} at $T = 26$ K, confirming that the sublimation energy flux is much larger than the conducted energy flux.

ORCID iDs

Naceur Bouziani https://orcid.org/0000-0002-3805-7120

References

Abplanalp, M. J., Frigge, R., & Kaiser, R. I. 2019, SciA, 5, eaaw5841
Baxter, E. J., Blake, C. H., & Jain, B. 2018, AJ, 156, 243
Bouziani, N., & Fanale, F. P. 1998, ApJ, 499, 463
Cussler, E. L. 2009, Diffusion: Mass Transfer in Fluid Systems (Cambridge: Cambridge Univ. Press)
Delsemme, A. H., & Miller, D. C. 1971, P&SS, 19, 1229
Farnham, T. 2021, ATel, 14759, 1
Fray, N., & Schmitt, B. 2009, P&SS, 57, 2053
Fulle, M., Blum, J., & Rotundi, A. 2020, A&A, 636, L3
Gautier, T., Danger, G., Mousis, O., et al. 2020, E&PSL, 531, 116011
Guilbert-Lepoutre, A., Besse, S., Mousis, O., et al. 2012, SSRv, 197, 271
Gundlach, B., Blum, J., Keller, H. U., et al. 2015, A&A, 583, A12

Hui, M.-T., Farnocchia, D., & Micheli, M. 2019, AJ, 157, 162
Jewitt, D. 2009, AJ, 137, 4296
Jewitt, D., Hui, M.-T., Mutchler, M., et al. 2017, ApJL, 847, L19
Jewitt, D., Agarwal, J., Hui, M.-T., et al. 2019a, AJ, 157, 65
Jewitt, D., Kim, Y., Luu, J., et al. 2019b, AJ, 157, 103
Jewitt, D., Kim, Y., Mutchler, M., et al. 2021, AJ, 161, 188
Kaiser, R. I., & Roessler, K. 1997, ApJ, 475, 144
Krupka, K. M., Robie, R. A., Hemingway, B. S., Kerrick, D. M., & Ito, J. 1985, AmMin, 70, 249
Królikowska, M., & Dybczyński, P. A. 2018, A&A, 615, A170
Luna, R., Satorre, M. Á., Santonja, C., & Domingo, M. 2014, A&A, 566, A27
Mayo Greenberg, J. 2002, SurSc, 500, 793
Mendis, D. A., & Brin, G. D. 1977, Moon, 17, 359
Moghaddam, R. N., & Jamiolahmady, M. 2016, Fuel, Elsevier, 173, 298
Prialnik, D., & Bar-Nun, A. 1988, Icar, 258, 272
Prialnik, D., & Bar-Nun, A. 1992, A&A, 258, L9
Prialnik, D., & Sierks, H. 2017, MNRAS, 469, S217
Sánchez, P., & Scheeres, D. J. 2014, M&PS, 49, 788
Shulman, L. M. 2004, A&A, 416, 187
Watson, K., Murray, B. C., & Brown, H. 1961, JGR, 66, 3033
Whipple, F. L. 1950, ApJ, 111, 375